A SLIDING-MESH STRATEGY BASED ON THE MIXING OF CONTINUOUS AND DISCONTINUOUS FINITE ELEMENT METHODS FOR COMPRESSIBLE FLOW PROBLEMS

Ezequiel J. López[a] and Gustavo A. Ríos Rodríguez[b]

[a]*Departamento de Mecánica Aplicada, Facultad de Ingeniería, Universidad Nacional del Comahue, CONICET, Buenos Aires 1400, 8300 Neuquén, Argentina, ezequiel.lopez@fain.uncoma.edu.ar*

[b]*Centro Internacional de Métodos Computacionales en Ingeniería (CIMEC), CONICET, Universidad Nacional del Litoral, Colectora RN 168/Paraje El Pozo, 3000 Santa Fe, Argentina, gusadrr@yahoo.com.ar*

Keywords: Sliding-mesh strategy, Discontinuous Galerkin method, internal combustion engine simulation.

Abstract. There are flow problems in which different parts of the domain are in relative motion. This occurs, for instance, in turbomachinery, in internal combustion engines with ports for gas exchange (two-stroke engines and rotary engines), etc. The computational simulation of such problems becomes simpler if the flow domain is split into sub-domains with different motion or deformation rate. These sub-domains could have a common boundary over which, due to the relative motion, they slide one with respect to the other. In this article a sliding-mesh strategy is presented, which is useful to solve the kind of problems cited above when the involved flow is compressible. The strategy is based on the use of standard (*i.e.*, continuous) finite elements at the interior of the domain and a layer of discontinuous elements at the 'sliding' surface between two adjacent sub-domains. It must be pointed out that the inter-element discontinuity appears between elements of neighbor sub-domains, which share a facet lying on the 'sliding' surface. Therefore, nonconformal meshes at sub-domain boundaries can be used. The solution is continuous across element faces lying inside each sub-domain. The finite element formulation applied at the interior of the sub-domains is stabilized by means of the Streamline-Upwind/Petrov-Galerkin (SUPG) technique. A shock-capturing term is added to the formulation in order to stabilize the computations in the presence of sharp gradients. At the discontinuous elements layer, an interior penalization Discontinuos Galerkin (DG) method is applied. The Lax-Friedrichs fluxes are used in this work in order to define the numerical fluxes arising in the DG method. For the penalization coefficients involved in the Lax-Friedrichs flux, the definitions given in the literature and modifications of them are tested. In some cases, due to the relative motion between sub-domains, the faces of the elements belonging to the discontinuous layer could change their location from the portion of surface shared by two adjacent sub-domains to another portion of the border where boundary conditions must be specified. These boundary conditions are enforced through numerical fluxes properly designed. Wall boundary conditions and open boundary conditions are addressed here. Some numerical examples are presented in order to show the performance of the proposed strategy.

1 INTRODUCTION

There are flow problems of great interest in engineering and scientific research where different parts of the domain are in relative motion. Typical examples are turbomachinery simulation and modeling of the gas exchange process in internal combustion engines with ports (two-stroke engines and rotary engines). In fact, the last application was the motivation for the present work. The computational simulation of the cited problems becomes simpler if the flow domain is split into sub-domains with different motion or deformation rate. These sub-domains could have a common boundary over which, due to the relative motion, they slide one with respect to the other.

For instance, some developments for the simulation of internal combustion engines with ports include special techniques as the snapper in KIVA-3 (Amsden, 1993). In this technique, a neighboring plane to the piston crown follows the piston movement. The placement of this plane is periodically updated due to the relocalization of the piston. The snapper technique is limited to square ports and, in addition, it requires horizontal grid lines in the pipes around the periphery of the cylinder. Sliding-mesh strategies that apply interpolation techniques on the interface between the sub-domains (Rai, 1987) are generalizations of the snapper, since they can handle non-conformal meshes at the inter-subdomain boundary surface. Also, these strategies extend the application field to other kind of problems besides the flow simulation through the ports of an internal combustion engine. Several interpolation techniques were proposed in the literature, including high order interpolation (see, for instance, Steijl and Barakos (2008)) and conservative approaches (Sánchez-Caja et al., 1999). In general, sliding-mesh methods based on direct interpolation are used in a Finite Volume Method context.

When the Finite Element Method (FEM) is applied to solve the kind of problems cited above, the mortar technique (Bernardi et al., 2005) is extensively used. This technique can handle the nonconformity of meshes at the interface between the sub-domains, and even to account for an overlapping nonconformity in the domain decomposition (Cai et al., 1999). The main drawback of the mortar methods is that continuity of the numerical solution at the sub-domain interface is enforced by Lagrange multipliers.

Since the interface among sub-domains can be seen as a discontinuity surface for the numerical solution, the transfer of information between the grids on each sub-domain can be performed applying the Discontinuous Galerkin (DG) Method. Domino (2010) proposes a method where standard (i.e. continuous) finite elements are used inside each sub-domain, and an interior penalization DG method is applied at the non-conformal interface. The method developed by Domino (2010) is applicable to the resolution of incompressible flow problems, where an equal-order pressure stabilized FEM is used inside the sub-domains. This method is an extension of the method for heat transfer calculation implemented within the Sierra/TH code at Sandia National Labs (Carnes and Copps, 2008).

The starting point for the strategy presented in this work is the proposal made by Domino (2010) adapted to compressible flows in an Arbitrary Lagrangian Eulerian (ALE) framework. Nevertheless, the original formulation is modified based on the results of the solved tests. In addition, a suitable redefinition of the numerical fluxes is proposed in order to account for the relative change in the position of elements between the sub-domain interface and the boundary of the own sub-domain.

The paper is organized as follows. In section §2, the Navier-Stokes equations for compressible viscous flows applying an ALE strategy are presented. Then the numerical formulation is stated, including the variational formulation, the definition used for the numerical fluxes, and

the treatment of the boundary conditions weakly imposed. In section §4 some implementation issues are described. The next section presents the numerical results, including subsonic and supersonic flow problems, comparison of solutions computed with the proposed strategy and the 'continuous' formulation, and a motored two-dimensional two-stroke engine. Conclusions and a proposal of some future works conclude the paper.

2 GOVERNING EQUATIONS

Let $\Omega_t \subset \mathbb{R}^{n_\mathrm{d}}$ be the spatial domain, where n_d is the number of space dimensions, and let Γ_t denote its boundary. The spatial and temporal coordinates are denoted by $\mathbf{x}$ and t, respectively. Subscript t denotes time dependence for the position of the domain and its boundary. The time interval is $(0, t_\mathrm{f}]$. In order to account for the domain deformation, the Arbitrary Lagrangian Eulerian (ALE) description is applied. In the ALE approach, two configurations of the system are considered: an instantaneous configuration $\Omega_t(\mathbf{x})$ and a reference configuration $\Omega_0(\boldsymbol{\zeta})$. Therefore, a mapping function between $\Omega_t(\mathbf{x})$ and $\Omega_0(\boldsymbol{\zeta})$ is defined as $\mathbf{x} = \mathbf{x}(\boldsymbol{\zeta}, t)$. Using the ALE strategy proposed by Donea et al. (1982), the Navier-Stokes equations governing the fluid flow in conservation form are

$$J^{-1}(J\mathbf{U}),_t + (\mathbf{F}_i^\mathrm{a} - w_i\mathbf{U}),_i - \mathbf{F}_{i,i}^\mathrm{d} = \mathbf{S} \quad \text{on } \Omega_t \times (0, t_\mathrm{f}], \quad i = 1, \ldots, n_\mathrm{d} \tag{1}$$

where $\mathbf{U} = [\rho,\ \rho\mathbf{u},\ \rho E]^T$ is the vector of conservative variables, ρ is the density, $\mathbf{u}$ is the flow velocity, E is the total energy per unit mass, and the superscript T indicates matrix transpose. $\mathbf{F}^\mathrm{a}$ and $\mathbf{F}^\mathrm{d}$ are the advective and viscous flux vectors respectively, defined as

$$\mathbf{F}^\mathrm{a} = \begin{bmatrix} \rho\mathbf{u} \\ \rho\mathbf{u} \otimes \mathbf{u} + p\mathbf{I} \\ (\rho E + p)\mathbf{u} \end{bmatrix}, \quad \mathbf{F}^\mathrm{d} = \begin{bmatrix} 0 \\ \mathbf{T} \\ \mathbf{T} \cdot \mathbf{u} - \mathbf{q} \end{bmatrix} \tag{2}$$

where p is the pressure, $\mathbf{T} = \mu[(\boldsymbol{\nabla}\mathbf{u}) + (\boldsymbol{\nabla}\mathbf{u})^T - 2/3(\boldsymbol{\nabla} \cdot \mathbf{u})\mathbf{I}]$ is the viscous stress tensor, $\mathbf{q} = -\kappa\boldsymbol{\nabla}T$ is the heat flux vector, and $\mathbf{I}$ is the second order identity tensor. μ is the dynamic viscosity of the fluid, κ is its thermal conductivity and T is the flow temperature. In eq. (1) $J = \det\left(\dfrac{\partial\mathbf{x}}{\partial\boldsymbol{\zeta}}\right)$, $w_i = \dfrac{dx_i}{dt}\bigg|_{\boldsymbol{\zeta}}$, and $\mathbf{S}$ is the source term.

The fluid is modeled as an ideal gas with particular constant R and specific heat ratio γ.

The system of governing equations is completed with the initial and boundary conditions. In regards to these latter, we assume that the whole boundary Γ_t admits the decomposition $\Gamma_t = \overline{\Gamma_g \cup \Gamma_h \cup \Gamma_f}$ such that $\overline{\Gamma_g \cap \Gamma_h \cap \Gamma_f} = \emptyset$, where Γ_g and Γ_h represent the portions of Γ_t where Dirichlet and Neumann type conditions are respectively imposed. Γ_f is the part of the boundary where dynamic boundary conditions are applied (see Storti et al. (2008)).

In the sequel, with the aim to simplify the notation, we will drop the subscript t from the symbol representing the problem domain Ω_t and its boundary Γ_t.

3 NUMERICAL FORMULATION

We consider that the whole domain Ω is split into two or more non-overlapping sub-domains such that some portions of their boundaries can slide one over the others. Figure 1 shows the case for two sub-domains which, for the sake of simplicity, is the one we consider in what follows. These sub-domains are labeled A and B, and we use the superscript α to denote anyone of them. The interface between sub-domains A and B is named Γ_{AB}.
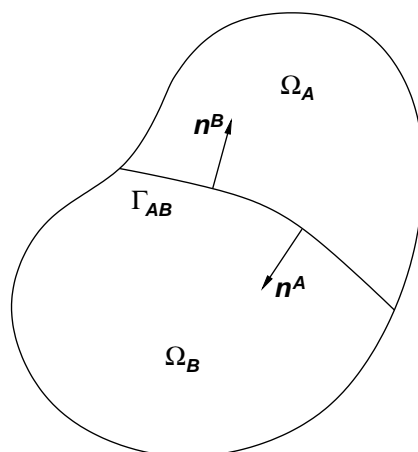
Figure 1: Flow domain split into two sub-domains Ω_A and Ω_B with an interface Γ_{AB}.

Suppose that sub-domain Ω_α is discretized into n_{el}^α finite elements Ω_α^e, $e = 1, 2, \ldots, n_{\mathrm{el}}^\alpha$. Based on these discretizations, the finite element function spaces for the trial solutions and the weighting functions $\mathscr{S}^{\alpha h}$ and $\mathscr{V}^{\alpha h}$, respectively, are defined as

$$
\begin{aligned}
\mathscr{S}^{\alpha h} &= \{\mathbf{U}^h | \mathbf{U}^h \in [\mathbf{H}^{1h}(\Omega_\alpha)]^{n_{\mathrm{dof}}}, \ \mathbf{U}^h|_{\Omega_\alpha^e} \in [P^1(\Omega_\alpha^e)]^{n_{\mathrm{dof}}}, \ \mathbf{U}^h = \mathbf{g} \text{ on } \Gamma_g \cap \partial\Omega_\alpha\} \\
\mathscr{V}^{\alpha h} &= \{\mathbf{W}^h | \mathbf{W}^h \in [\mathbf{H}^{1h}(\Omega_\alpha)]^{n_{\mathrm{dof}}}, \ \mathbf{W}^h|_{\Omega_\alpha^e} \in [P^1(\Omega_\alpha^e)]^{n_{\mathrm{dof}}}, \ \mathbf{W}^h = \mathbf{0} \text{ on } \Gamma_g \cap \partial\Omega_\alpha\}
\end{aligned}
\tag{3}
$$

$\mathbf{H}^{1h}(\Omega_\alpha)$ being the finite dimensional Sobolev functional space over Ω_α, and $\mathbf{g}$ the Dirichlet boundary condition vector. n_{dof} stands for the number of degrees of freedom and $P^1(\Omega_\alpha^e)$ represents the space of piecewise linear polynomials on Ω_α^e.

Then, the discrete variational problem is written as follows:

Find $\mathbf{U}^{\alpha h} \in \mathscr{S}^{\alpha h}$ such that $\forall\, \mathbf{W}^{\alpha h} \in \mathscr{V}^{\alpha h}$

$$
\begin{aligned}
&\int_{\Omega_\alpha^h} \mathbf{W}^{\alpha h} \left(\mathbf{U}_{,t}^{\alpha h} - \mathbf{S}^{\alpha h} \right) d\Omega - \int_{\Omega_\alpha^h} \mathbf{W}_{,i}^{\alpha h}[(\mathbf{F}_i^{ah,\alpha} - w_i^{\alpha h}\mathbf{U}^{\alpha h}) - \mathbf{F}_i^{dh,\alpha}]d\Omega \\
&+ \sum_{e=1}^{n_{\mathrm{el}}^\alpha} \int_{\Omega_\alpha^e} \boldsymbol{\tau}(\mathbf{A}_k^{\alpha h} - w_k^{\alpha h}\mathbf{I})^T \mathbf{W}_{,k}^{\alpha h} \left[\mathbf{U}_{,t}^{\alpha h} + (\mathbf{A}_i^{\alpha h} - w_i^{\alpha h}\mathbf{I})\mathbf{U}_{,i}^{\alpha h} - \mathbf{F}_{i,i}^{dh,\alpha} - \mathbf{S}^{\alpha h} \right] d\Omega^e \\
&+ \sum_{e=1}^{n_{\mathrm{el}}^\alpha} \int_{\Omega_\alpha^e} \delta_{\mathrm{sc}} \mathbf{W}_{,i}^{\alpha h} \mathbf{U}_{,i}^{\alpha h} d\Omega^e + \int_{\partial\Omega_\alpha^h \backslash \Gamma_{AB}^h} \mathbf{W}^{\alpha h}[(\mathbf{F}_i^{ah,\alpha} - w_i^{\alpha h}\mathbf{U}^{\alpha h}) - \mathbf{F}_i^{dh,\alpha}]n_i^\alpha d\Gamma \\
&+ \int_{\Gamma_{AB}^h} \mathbf{W}^{\alpha h}[\hat{\mathbf{F}}_n^a(\alpha, \beta) - \hat{\mathbf{F}}_n^d(\alpha, \beta)]d\Gamma = \mathbf{0}
\end{aligned}
\tag{4}
$$

where α indicates evaluation of variables at the 'current' mesh and β represents evaluation at the 'opposite' mesh. n_i, $i = 1, \ldots, n_d$, are the components of the outward unit normal vector to the boundary domain and $\mathbf{A}_i = \partial\mathbf{F}_i^a/\partial\mathbf{U}$, $i = 1, \ldots, n_d$, are the advective Jacobian matrices (Hirsch, 1990).

The first three terms in (4) are the standard SUPG (Streamline Upwind/Petrov-Galerkin) formulation, where the flux term is integrated by parts. This integration by parts leads to an integral on the boundary that is split into an integral over the sliding surface and an integral on the remaining boundary (sixth and fifth terms in (4) respectively). In the integral over Γ_{AB}

the flux vectors are replaced by numerical fluxes, as usual in the DG methods (Li, 2006). The fourth integral includes the shock capturing terms that stabilize the computations in the presence of sharp gradients, δ_{sc} being the coefficient of shock capturing.

Since we are interested in the resolution of compressible flows in the whole range of Mach numbers, the intrinsic time tensor $\boldsymbol{\tau}$ in the stabilization term is computed as proposed by López et al. (2012), as follows (see also López et al. (2008) and López (2009))

$$\boldsymbol{\tau} = \max\left[\mathbf{0}, \boldsymbol{\tau}_a - \boldsymbol{\tau}_d - \boldsymbol{\tau}_\delta\right] \tag{5}$$

where (Aliabadi et al., 1993)

$$\boldsymbol{\tau}_d = \frac{\sum_{j=1}^{n_{\text{d}}} \tilde{\beta}_j^2 \text{diag}(\mathbf{K}_{jj})}{(c + \|\mathbf{u}\|)^2}\mathbf{I}$$
$$\boldsymbol{\tau}_\delta = \frac{\delta_{\text{sc}}}{(c + \|\mathbf{u}\|)^2}\mathbf{I} \tag{6}$$

and

$$\boldsymbol{\tau}_a = \frac{\partial \mathbf{U}}{\partial \mathbf{Q}}\tilde{\boldsymbol{\tau}}_{\text{v}}\boldsymbol{\Gamma}_{\text{v}}^{-1} \tag{7}$$

c is the sonic speed, $\tilde{\beta} = \boldsymbol{\nabla}\|\mathbf{U}\|^2/\|\boldsymbol{\nabla}\|\mathbf{U}\|^2\|$, $\mathbf{K}_{ij}$ is the diffusivity Jacobian matrix, which satisfies $\mathbf{K}_{ij}\partial \mathbf{U}/\partial x_j = \mathbf{F}_i^{\text{d}}$, and $\|\cdot\|$ represents the Euclidean norm.

In the expression for $\boldsymbol{\tau}_a$, $\mathbf{Q} = [p, \mathbf{u}, T]^T$ is the vector of viscous variables (Choi and Merkle, 1993),

$$\boldsymbol{\Gamma}_{\text{v}} = \begin{bmatrix} \dfrac{1}{\beta M_{\text{r}}^2} & \mathbf{0} & 0 \\[2mm] \dfrac{\mathbf{u}}{\beta M_{\text{r}}^2} & \rho\mathbf{I} & \mathbf{0} \\[2mm] \dfrac{\rho e + p}{\rho\beta M_{\text{r}}^2} - 1 & \rho\mathbf{u} & \dfrac{\gamma\rho R}{\gamma - 1} \end{bmatrix} \tag{8}$$

is a preconditioning matrix, and $\tilde{\boldsymbol{\tau}}_{\text{v}} = \tau_{\text{v}}\mathbf{I}$.

In eq. (8), $M_{\text{r}} = \min(1, \max(\sqrt{M^2 + CFL_c^{-2}}, M_\epsilon))$ is a reference Mach number, $\beta = zc^2$, and e is the internal energy per unit mass. $M = \|\mathbf{u}\|/c$ is the Mach number, $CFL_c = c\Delta t/h$ is the CFL (Courant-Friedrichs-Levy) number based on the sound speed, Δt is the time step, h is a characteristic element length, and M_ϵ is a cut-off of the Mach number included in order to avoid singularities in the vicinity of stagnation points. In this work, $M_\epsilon = 1 \times 10^{-6}$ was used. In addition, $z = \max(1, z_{\text{vis}})$, with

$$z_{\text{vis}} = \frac{Re_h^{-1}(Re_h^{-1} - 1)}{M_{\text{r}}^2[Re_h^{-1} - 1 + c^2/(\mathbf{u}\cdot\mathbf{s})^2]} \tag{9}$$

where $Re_h = \rho\|\mathbf{u}\|h/\mu$ is the cell Reynolds number, and $\mathbf{s}$ is the unit vector aligned with the flow velocity. On the other hand,

$$\tau_{\text{v}} = \left[\left(\frac{\frac{1}{2}[\|\mathbf{u}\|(1 + \beta M_{\text{r}}^2/c^2) + c']}{h/2}\right)^2 + \left(\frac{2}{\Delta t}\right)^2\right]^{-1/2} \tag{10}$$

$c' = \sqrt{\|\mathbf{u}\|^2\left(1 + \dfrac{\beta M_{\text{r}}^2}{c^2}\right)^2 + 4\beta M_{\text{r}}^2\left(1 - \dfrac{\|\mathbf{u}\|^2}{c^2}\right)}$ being the pseudo-acoustic speed. The characteristic element length is computed as the element length in the direction of the streamline

$h = 2(\sum_{a=1}^{n_{\text{en}}} \|\mathbf{s} \cdot \boldsymbol{\nabla} N_a\|)^{-1}$, where N_a is the trial function associated with the node a and n_{en} is the number of nodes in the element.

An isotropic operator proposed by Tezduyar and Senga (2004) is used for the shock capturing term, which is computed as follows. Let $\mathbf{j} = \boldsymbol{\nabla}\rho^h/\|\boldsymbol{\nabla}\rho^h\|$ a unit vector oriented with the density gradient and the characteristic length $h_{JGN} = 2(\sum_{a=1}^{n_{\text{en}}} \|\mathbf{j} \cdot \boldsymbol{\nabla} N_a\|)^{-1}$. The isotropic shock capturing factor included in equation (4) is then defined as

$$\delta_{\text{sc}} = \frac{h_{JGN}}{2} u_{\text{char}} \left(\frac{\|\boldsymbol{\nabla}\rho^h\| h_{JGN}}{\rho_{\text{ref}}} \right)^{\beta^*} \tag{11}$$

where $u_{\text{char}} = \|\mathbf{u}\| + c$ is the characteristic velocity, ρ_{ref} is the density interpolated at the Gaussian point, and β^* is a parameter that can be taken as 1 or 2 according to the sharpness of the discontinuity to be captured.

There are many choices for the numerical fluxes, see, for instance, Cockburn et al. (2000). In this work we use the Lax-Friedrichs approach for the advective flux

$$\hat{\mathbf{F}}_n^{\text{a}}(\alpha, \beta) = \frac{1}{2}\{[(\mathbf{F}_i^{\text{a}h,\,\alpha} - w_i^{\alpha h}\mathbf{U}^{\alpha h})n_i^\alpha - (\mathbf{F}_i^{\text{a}h,\,\beta} - w_i^{\beta h}\mathbf{U}^{\beta h})n_i^\beta] + \lambda^{\text{a},\alpha}(\mathbf{U}^{\alpha h} - \mathbf{U}^{\beta h})\} \tag{12}$$

where $\lambda^{\text{a},\alpha} = |\mathbf{u}^\alpha \cdot \mathbf{n}^\alpha| + c^\alpha$. A similar expression is used for the computation of the numerical diffusive flux

$$\hat{\mathbf{F}}_n^{\text{d}}(\alpha, \beta) = \frac{1}{2}[(\mathbf{F}_i^{\text{d}h,\,\alpha}n_i^\alpha - \mathbf{F}_i^{\text{d}h,\,\beta}n_i^\beta) + \lambda^{\text{d},\alpha}(\mathbf{U}^{\alpha h} - \mathbf{U}^{\beta h})] \tag{13}$$

where $\lambda_1^{\text{d},\alpha} = 0$, $\lambda_{2,\dots,n_{\text{d}}+1}^{\text{d},\alpha} = C^{\text{d}}\mu_{\text{eff}}^\alpha/\rho^\alpha h^\alpha$ and $\lambda_{n_{\text{d}}+2}^{\text{d},\alpha} = C^{\text{d}}\kappa_{\text{eff}}^\alpha/\rho^\alpha c_p^\alpha h^\alpha$. h is taken as the length of the element in the normal direction to the discontinuous surface, c_p is the specific heat at constant pressure and C^{d} is a user-defined coefficient. μ_{eff} and κ_{eff} are the effective viscosity and the effective thermal conductivity, which are the sum of their respective laminar and turbulent values.

Domino (2010) includes in the formulation an interior penalization term of the form

$$\int_{\Gamma_{AB}^h} \mathbf{W}_{,i}^{\alpha h} n_i^\alpha \lambda^{IP}(\mathbf{U}^{\alpha h} - \mathbf{U}^{\beta h}) d\Gamma, \tag{14}$$

where λ^{IP} is an interior penalization coefficient. Domino claims that the addition of this term is critical in generalized fluids problems, particularly for the continuity equation. However, we do not find any advantage in the solution accuracy because of the inclusion of this term, at least for the problems that we solved.

Time derivatives are discretized using the backward Euler scheme.

3.1 Boundary conditions

Since the problem domain is deformable, the interface between sub-domains Γ_{AB}, or some portion of it, could change its position from the interior to the boundary of the domain. In this case, for those elements on Γ_{AB} the boundary conditions are weakly imposed through the numerical fluxes. In order to compute these fluxes, a suitable 'opposite' state must be defined (Atkins, 1997). Two types of boundary condition were implemented in this work: solid wall and far-field.

In what follows, we use the superscript A to denote variables at the 'current' mesh, while the superscript B is used to denote variables at the 'opposite' mesh.

3.1.1 Solid wall boundary condition

For the computation of the numerical advective flux we follow the proposal of Collis (2002). If $\mathbf{n}^A$ is the normal unit vector to the wall, we define the projection $\mathbf{p}^A$ of the flow velocity onto the tangential direction to the wall as follows

$$\mathbf{p}^A = \mathbf{u}^A - (\mathbf{u}^A \cdot \mathbf{n}^A)\mathbf{n}^A \tag{15}$$

Then, the state used to compute the numerical advective flux is

$$\mathbf{U}^B = \begin{bmatrix} \rho^A \\ \rho^A \mathbf{p}^A \\ \rho^A e^A + \frac{1}{2}\rho^A \|\mathbf{p}^A\|^2 \end{bmatrix} \tag{16}$$

This state enforces the non-penetration condition on the wall.

In the case of the numerical diffusive flux, we must distinguish between a no-slip condition and a 'law-of-the-wall' turbulent condition. In the former case the state is given by

$$\mathbf{U}^B = \begin{bmatrix} \rho^A \\ \rho^A \mathbf{u}_w \\ \rho^A c_v T_w + \frac{1}{2}\rho^A \|\mathbf{u}_w\|^2 \end{bmatrix} \tag{17}$$

where $\mathbf{u}_w$ is the velocity of the wall, T_w is the wall temperature, and c_v is the specific heat at constant volume. The diffusive flux in equation (13) is evaluated with the state $\mathbf{U}^B$ using the expression (2).

For a turbulent 'law of the wall', the 'opposite' state is computed as

$$\mathbf{U}^B = \begin{bmatrix} \rho^A \\ \rho^A(\mathbf{u}^A - \mathbf{u}_w) \\ \rho^A e^A + \frac{1}{2}\rho^A \|\mathbf{u}^A - \mathbf{u}_w\|^2 \end{bmatrix}, \tag{18}$$

while the projection of the diffusive flux onto the normal direction to the wall is given by

$$\mathbf{F}^{\mathrm{d},B} \cdot \mathbf{n}^B = \begin{bmatrix} 0 \\ -\rho^A u_*^2 \dfrac{\mathbf{u}^A - \mathbf{u}_w}{\|\mathbf{u}^A - \mathbf{u}_w\|} \\ -\rho^A u_*^2 \|\mathbf{u}^A - \mathbf{u}_w\| + q_w \end{bmatrix} \tag{19}$$

u_* being the so-called friction velocity. This velocity is computed with empirical relations between the mean fluid speed relative to the wall $\|\mathbf{u} - \mathbf{u}_w\|$ and the normal distance to the wall y as

$$y^+ = f(u^+) \tag{20}$$

where $y^+ = \rho y u_*/\mu$ and $u^+ = \|\mathbf{u} - \mathbf{u}_w\|/u_*$. In eq. (19), q_w is the heat flux normal to the wall. This heat flux can be an imposed data or be estimated applying the Reynolds analogy between linear momentum and energy (Wilcox, 2002).

When a wall boundary condition is weakly applied via the numerical fluxes, it is possible to add a penalization term to the formulation in order to further enforce the non-penetration condition or the no-slip condition. This term is computed as follows

$$\int_{\Gamma_{AB} \cap \Gamma_w} \mathbf{W}^A \mathbf{M}^* (\mathbf{U}^{Ah} - \mathbf{U}_w) d\Gamma \tag{21}$$

where Γ_w is the portion of the boundary domain on which the wall boundary condition is applied, $\mathbf{U}_w = [0,\, \rho\mathbf{u}_w,\, 0]^T$, and

$$\mathbf{M}^* = \frac{1}{\epsilon} \begin{bmatrix} 0 & \mathbf{0} & 0 \\ \mathbf{0} & \mathbf{PMP}^{-1} & \mathbf{0} \\ 0 & \mathbf{0} & 0 \end{bmatrix} \tag{22}$$

In this equation, ϵ is a small enough parameter, $\mathbf{P} = [\mathbf{n}^A\ \mathbf{t}_1^A\ \mathbf{t}_2^A]$ (in the three dimensional case), $\mathbf{t}_1^A$ being a vector tangent to the wall, and $\mathbf{t}_2^A = \mathbf{n}^A \times \mathbf{t}_1^A$. For a no-slip boundary condition $\mathbf{M} = \mathbf{I}$, while for a non-penetration condition $\mathbf{M} = \mathrm{diag}(1,\, 0,\, 0)$, which is valid for a three dimensional problem.

3.1.2 Far-field boundary condition

The far-field is assumed to have a known reference state (the 'free-stream state') $\mathbf{U}_{\mathrm{ref}}$. This state is used to compute the numerical advective flux. The numerical diffusive flux is assumed to be zero.

4 IMPLEMENTATION ISSUES

As noted above, although the term added to the formulation is a surface integral, a strip of volumetric elements is needed in order to compute the gradient of the shape function. This term involves states at the 'current' mesh (which is named mesh A in this explanation) and at the 'opposite' mesh (hereon denominated mesh B). Therefore for each integration point, the state at the opposite mesh is found by projecting the point coordinates onto the opposite surface in the normal direction, as follows. Given the coordinates of the integration point $\mathbf{x}_{gp}^A$, the N nearest geometric center of the surface elements in the opposite mesh are searched. Typically, N is set between 5 and 10. This search is performed using the library ANN (Mount and Arya, 1998-2010). Since we use isoparametric elements, the goal is to find the element in the mesh B such that

$$\mathbf{x}_{pg}^A + \lambda\mathbf{n}^A = \sum_{j=1}^{n_{\mathrm{en}}^B} \mathbf{x}_j^B N_j^B(\boldsymbol{\xi}_{ip}) \tag{23}$$

where λ is an *a priori* unknown coefficient, n_{en}^B is the number of nodes in the surface elements of mesh B, $\boldsymbol{\xi}_{ip}$ are the local element coordinates of the interpolation point, N_j^B is the shape function associated to the node j in the surface element of the mesh B, and $\mathbf{x}_j^B$ are the coordinates of the nodes. The coefficient λ can be eliminated from the last equation, giving

$$\lambda = \sum_{j=1}^{n_{\mathrm{en}}^B} \frac{\mathbf{x}_j^B \cdot \mathbf{n}^A}{\|\mathbf{n}^A\|^2} N_j^B(\boldsymbol{\xi}_{ip}) - \frac{\mathbf{x}_{pg}^A \cdot \mathbf{n}^A}{\|\mathbf{n}^A\|^2} \tag{24}$$

Then, replacing eq. (24) in eq.(23) for each element in the set of 'nearest' elements, the resulting expression is used to obtain the local coordinates $\boldsymbol{\xi}_{ip}$. The projection of $\mathbf{x}_{pg}^A$ over the mesh B is verified in the element such that

$$0 \leq N_j^B(\boldsymbol{\xi}_{ip}) \leq 1, \quad j = 1,\ldots,n_{\mathrm{en}}^B \tag{25}$$

If condition (25) is not satisfied for none of the 'nearest' elements, it is assumed that a boundary condition must be applied on the opposite side. By the time, we can apply either a wall boundary condition or a free-stream boundary condition.

Finally, the state at the projected point and its derivatives are computed using the shape functions of the volumetric element, i.e. an element that belongs to the strip of elements adjacent to the sliding surface.

Given that we use an implicit solution method, the time instant at which the opposite mesh state is evaluated must be appropriately chosen. Evaluation at the current time step would be impractical because we use a Newton-like scheme for the resolution of the non-linear system, and therefore, each nodal state at the current mesh could be dependent on the state of the whole set of nodes that belong to the strip of elements in the opposite mesh. This occurs, for instance, in the simulation of turbomachinery, which is a typical application of the sliding-mesh techniques. In this work we use a staged strategy, where an additional loop of stages is included between the Newton loop and the time loop. The first stage is initialized with the state at the previous time step and then it is updated with the converged solution of the non-linear loop. In practice we use 1 or 2 stages, reaching a good equilibrium between accuracy and computational cost.

5 NUMERICAL EXAMPLES

The solved cases presented in this section were chosen in order to show the performance of the sliding-mesh technique in different type of applications. For the whole set of problems, it was used $C^{\mathrm{d}} = 1$ in equation (13).

5.1 Discharge of a reservoir to the atmosphere

In this test, the discharge of a reservoir to the atmosphere through a straight pipe is simulated. The length and diameter of the pipe are $L = 10$ m and $D = 1$ m. The gas is modeled as ideal, with particular constant $R = 287$ kJ/kg·K and specific heat ratio $\gamma = 1.4$. The state of the gas inside the reservoir is constant, with pressure $p_0 = 120$ kPa and temperature $T_0 = 300$ K. The atmospheric pressure is $p_a = 100$ kPa. Initially, the gas into the pipe is at rest and at the same pressure and temperature as the gas inside the reservoir. At $t = 0$ sec. the pipe end connected to the atmosphere is suddenly open. Diffusion effects are neglected. In order to simplify the problem, at the pipe end connected to the reservoir (left side) the density and the pressure are assumed constant throughout the simulation. On the other end of the pipe (right side), the atmospheric pressure is applied as boundary condition.

The aim of this simulation is to compare the solutions computed with the 'continuous' formulation and the 'discontinuous' one. In order to perform the last calculation, the domain is split into two sub-domains at the midpoint of the pipe. In both cases the domain is discretized with a structured mesh of quadrangles with side length $h = 0.1$ m. The time step used in the simulation is $\Delta t = 1 \times 10^{-3}$ sec.

Figure 2 shows the density at the midpoint of the pipe for both the continuous and discontinuous formulations. This latter was performed with 1, 2, and 3 stages of the additional loop used for the evaluation of the opposite state. If one stage is used, Fig. 2 shows that there exists a difference between the solutions from the left and right sub-domains. On the other hand, if two or more stages are applied, then it does not exist an appreciable difference between the left-side and right-side solutions. Figures 3 and 4 present analogous results for the axial flow velocity and the pressure, respectively.

It can be noted from the figures that there is a dephasing among the solutions obtained with the continuous formulation and those computed with the discontinuous strategy. This dephasing increases with the simulation time, and it reduces when the number of stages increases.
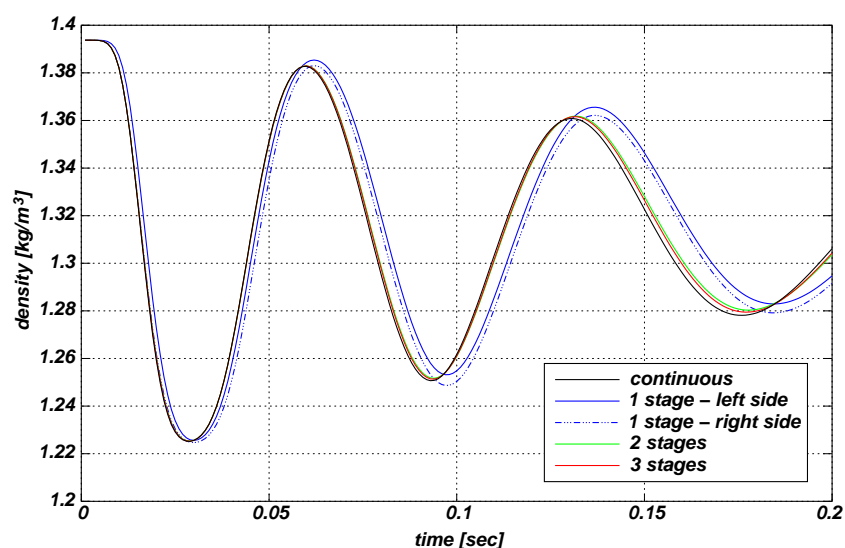
Figure 2: Density at the midpoint of the pipe for the discharge of a reservoir to the atmosphere problem.
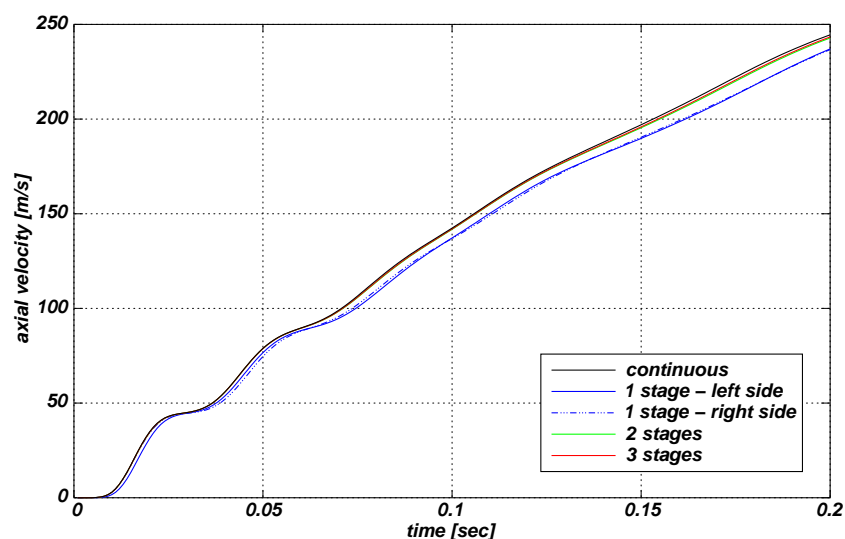

Figure 3: Axial velocity at the midpoint of the pipe for the discharge of a reservoir to the atmosphere problem.

However, the improvement reached with the increase in the number of stages is marginal. For instance, the solution with three stages approaches to the solution with two stages rather than to the continuous solution. Along with the dephasing of solutions there is a difference in the amplitude of the waves, which also increases in time.

5.2 Supersonic backward facing step

This case was taken from Woodward and Colella (1984) and consists of simulating an inviscid supersonic flow inside a two-dimensional wind tunnel with a step opposite to the flow direction, as shown in Fig. 5. The geometrical dimensions of the tunnel are: $H = 1$, $L = 3$, $a = 0.6$ and $b = 0.2$.

Initially, it is assumed that the tunnel is filled with a gas having a particular constant $R = 1$ and specific heat ratio $\gamma = 1.4$. Also, it is considered that its state is spatially constant, with: $\rho_0 = 1.4$, $p_0 = 1$, and $\mathbf{u}_0 = [3, 0]^T$. During the simulation, the state of the gas at the inlet surface (left boundary) is kept constant, equal to its initial values. At the outlet surface (right boundary)
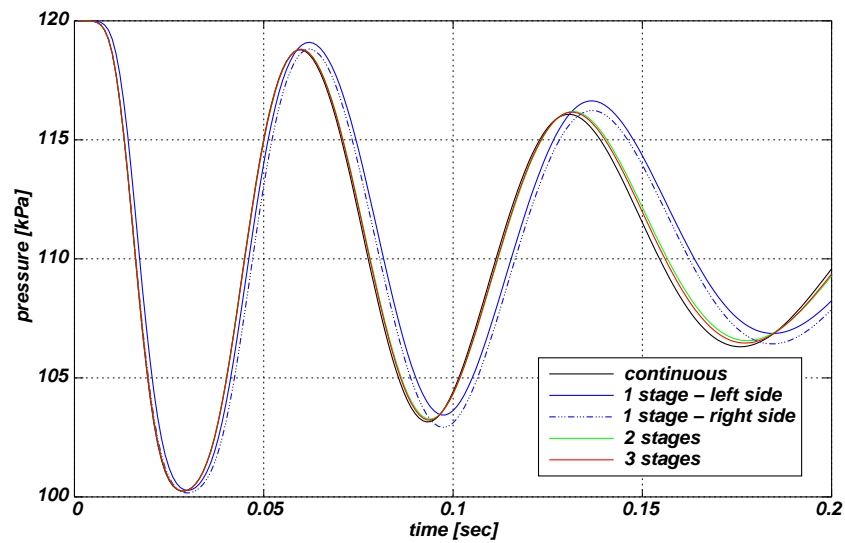
Figure 4: Pressure at the midpoint of the pipe for the discharge of a reservoir to the atmosphere problem.
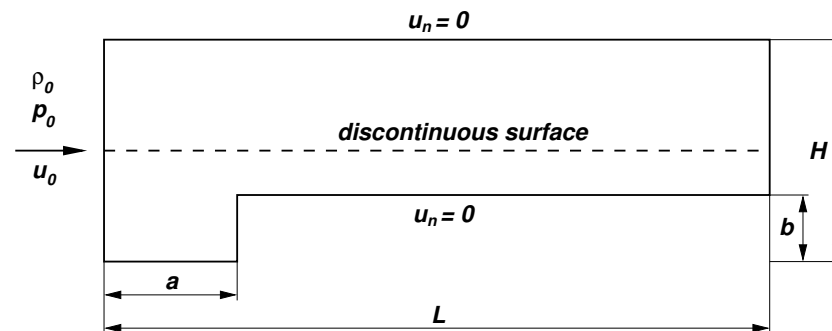
Figure 5: Sketch of the wind tunnel geometry for the supersonic backward facing step problem.

no condition is imposed because the flow is always supersonic (Woodward and Colella, 1984). Over the bottom and top walls the normal velocity component is set equal to zero.

The goal of this simulation is to evaluate the performance of the sliding-mesh technique in a problem with strong discontinuities, in order to assess the design of the numerical fluxes. Hence, the fluid dynamic equations are solved by applying both the 'continuous' and 'discontinuous' formulations. Two stages are used for the evaluation of the state in this latter.

The problem domain is split with an artificial surface at $y = H/2$ as shown in Fig. 5. The bottom sub-domain is discretized with a mesh of uniform quadrangles ($h = 1/80$), while in the upper sub-domain a mesh with triangular elements ($h = 1/85$) is used. The time step used for the simulation is $\Delta t = 1 \times 10^{-2}$. In order to minimize the diffusive effect of the shock-capturing term, the shock-capturing parameter is multiplied by the coefficient $c_\delta = 0.1725$.

Figure 6 presents the density field at several time instants for the solutions computed with both formulations. From this figure it can be observed that the main differences between the solutions computed with both strategies are located at the discontinuous surface, specially at the first time instants.

In order to make a more accurate comparison of both solutions, figures 7 to 9 show the computed flow fields at the discontinuous surface for the time instants 0.5, 2.0 and 4.0. The major differences appear in the first part of the time interval, particularly for the density and the flow velocity component in the horizontal direction (u velocity). Also, there are differences
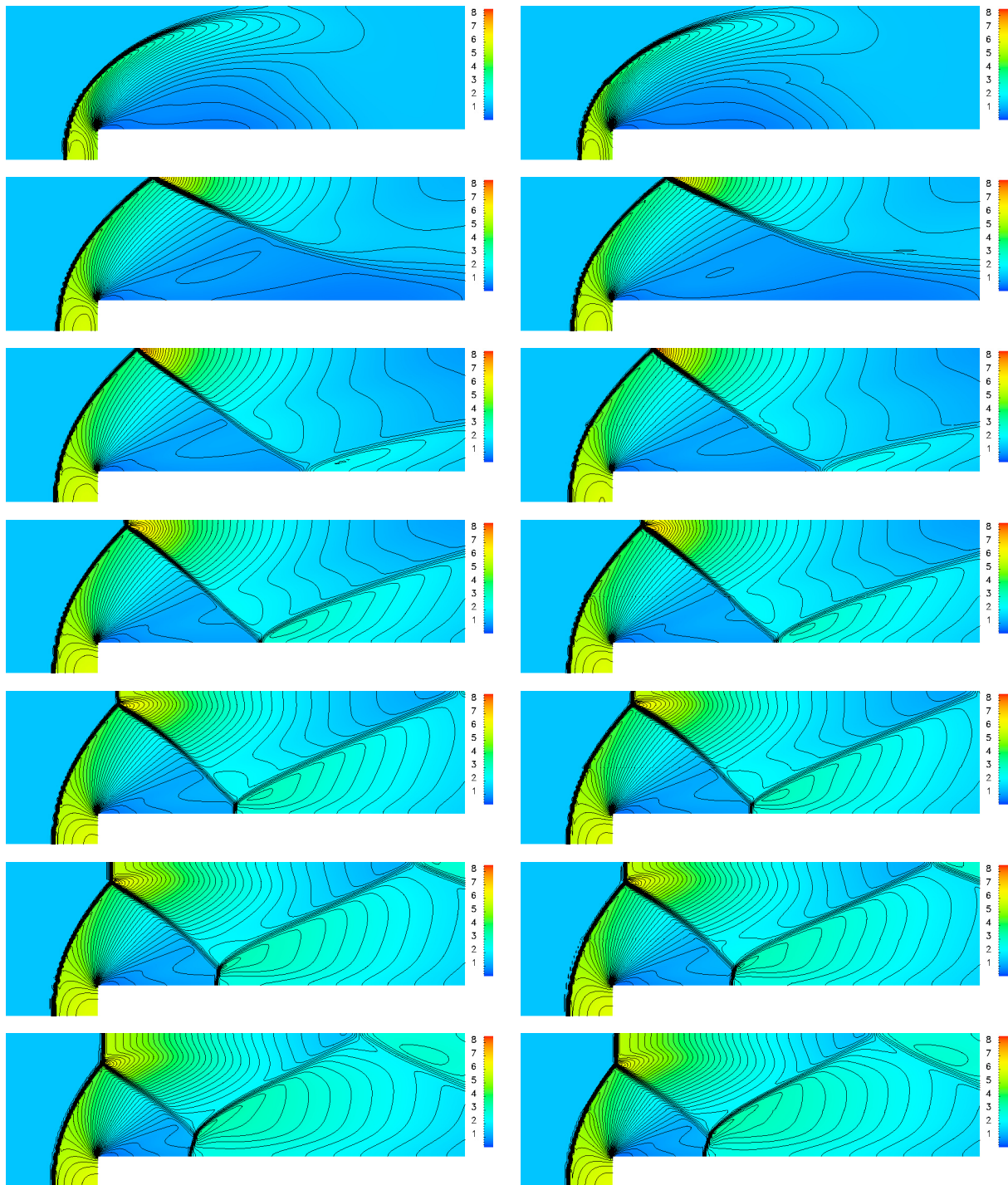
Figure 6: Density field for the supersonic backward facing step problem. Left: solution of the continuous formulation, right: solution of the discontinuous formulation using two stages. From top to bottom, times 0.5, 1.0, 1.5, 2.0, 2.5, 3.0, and 4.0.

located around the positions of the shocks, specially for the weaker ones.

5.3 Two-dimensional two-stroke engine

This test is representative of the kind of problems in which we are interested. Although it shows an engine with an oversimplified geometry, it holds the main features of a two-stroke
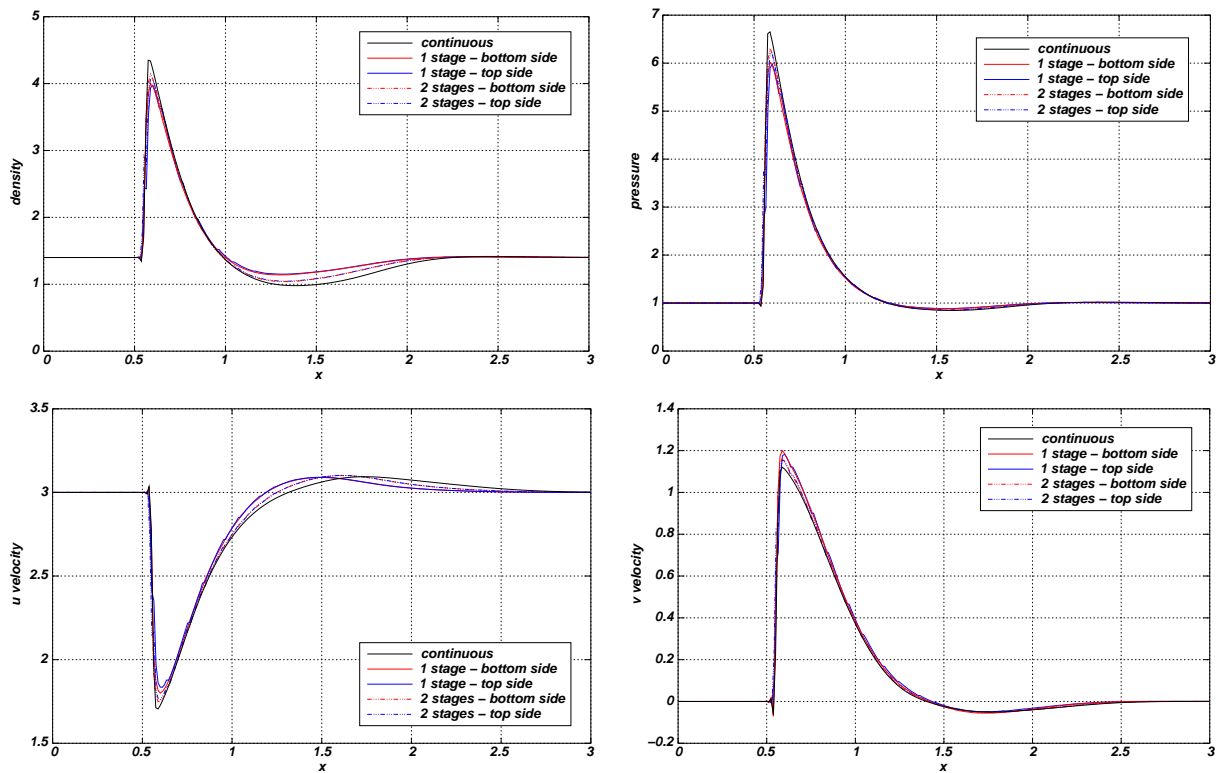
Figure 7: Density (top, left), pressure (top, right), horizontal velocity (bottom, left), and vertical velocity (bottom, right) at the interface $y = H/2$ for the supersonic backward facing step problem. Solution at time 0.5.
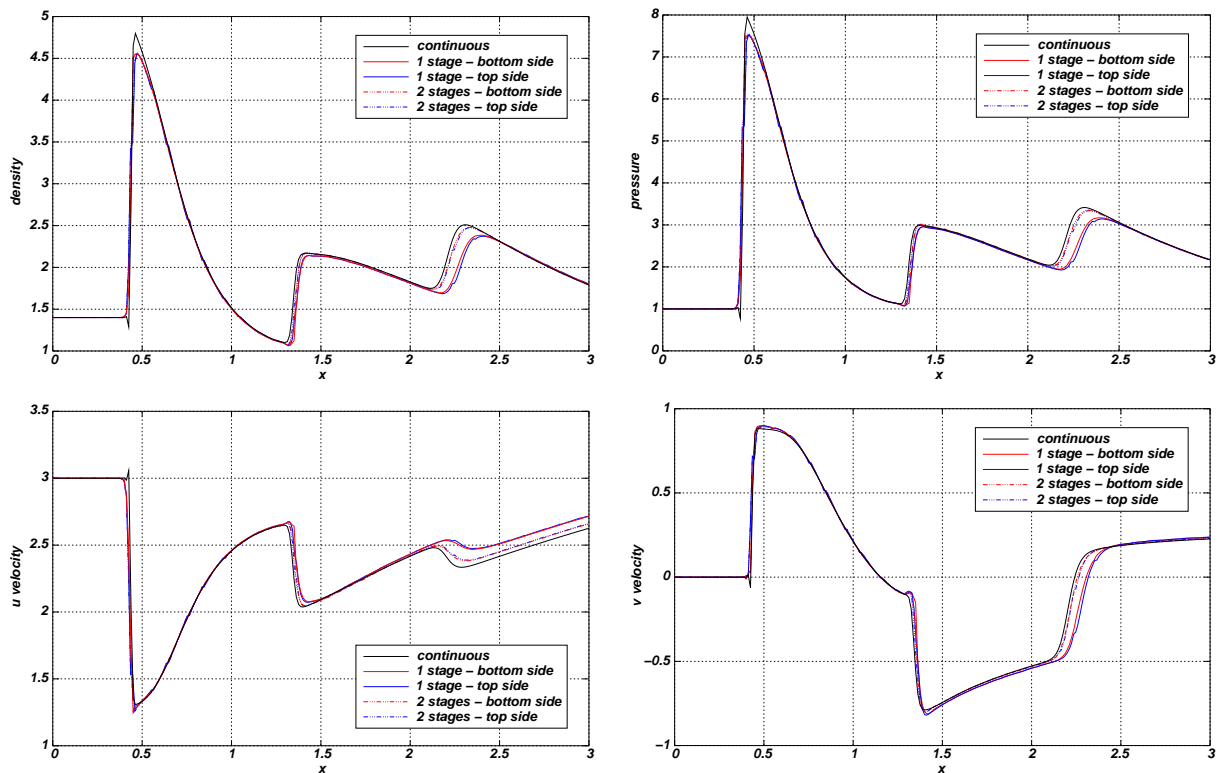
Figure 8: Density (top, left), pressure (top, right), horizontal velocity (bottom, left), and vertical velocity (bottom, right) at the interface $y = H/2$ for the supersonic backward facing step problem. Solution at time 2.0.
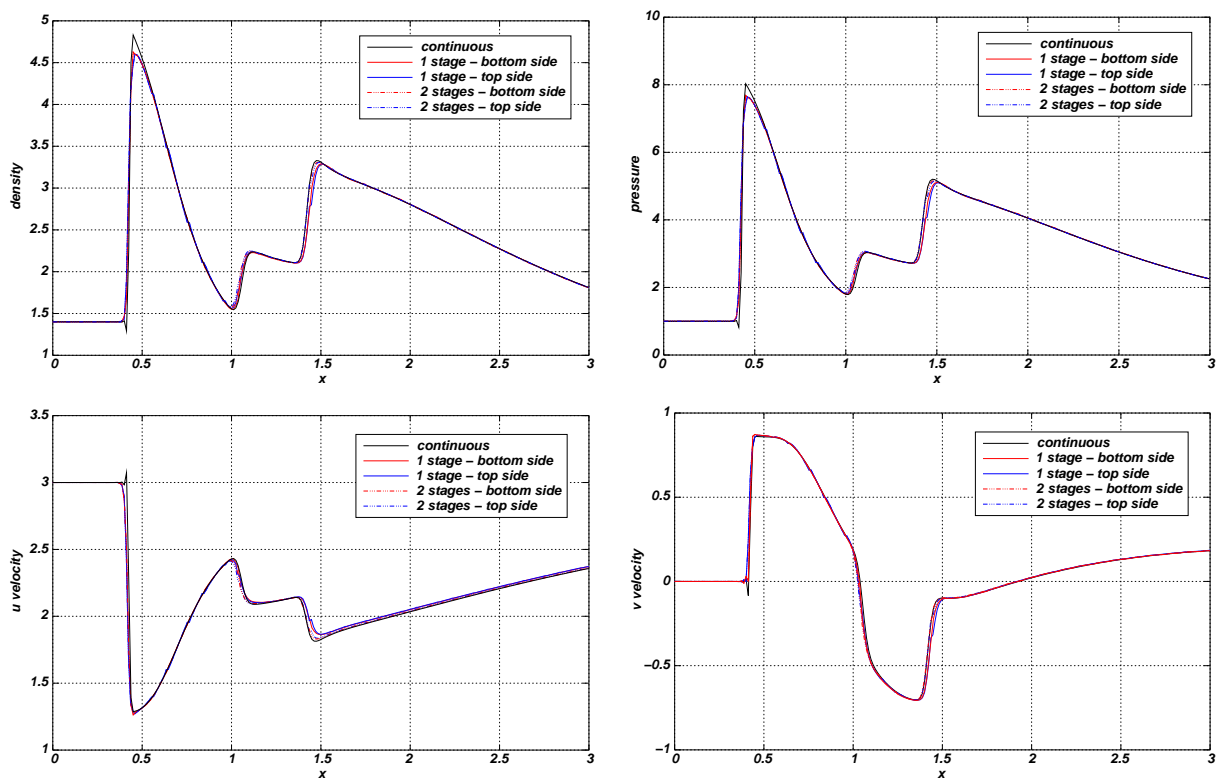
Figure 9: Density (top, left), pressure (top, right), horizontal velocity (bottom, left), and vertical velocity (bottom, right) at the interface $y = H/2$ for the supersonic backward facing step problem. Solution at time 4.0.

engine from the point of view of the application of the sliding-mesh technique presented in this work. Figure 10 outlines the main geometric dimensions of the engine, which are: $B = 100$ mm, $H_i = 35$ mm, $H_e = 45$ mm, the stroke is $S = 100$ mm, the connecting rod length is $l = 125$ mm, and the compression ratio is $r_c = 9$. The simulated lengths of both the intake pipe and the exhaust pipe are 50 mm. The engine is under motored conditions and its speed is 1000 rpm. The crank angle is referenced to the top center (TC) position of the piston. Therefore, with this reference angle, the exhaust port opens at $83.9°$ and closes at $276.1°$, while the intake port opens at $95.35°$ and closes at $264.65°$. The operating gas has $R = 287$ kJ/kg·K, $\gamma = 1.4$, dynamic viscosity $\mu = 1 \times 10^{-5}$ Pa·s and thermal conductivity $\kappa = 1 \times 10^{-3}$ W/K·m.

The cylinder is discretized with 11300 quadrangular elements, while for the intake and exhaust pipes 1750 and 2250 quadrangles are used. The mesh has a grading toward the walls, with a mean element size near the wall of 0.35 mm. Due to the simplicity of the geometry and the boundary movement, mesh dynamics is solved using an algebraic law following a linear distribution with respect to the position of piston at TC. Turbulent 'law of the wall' boundary conditions are applied over solid walls, and on the inlet and outlet surfaces dynamic boundary conditions are used (see Storti et al. (2008)). Constant reference states are assumed at the inlet (U_i) and oulet (U_e), with $U_i = [1.2195\,\text{kg/m}^3,\ \mathbf{0}\,\text{m/s},\ 105\,\text{kPa}]^T$ and $U_e = [1.1034\,\text{kg/m}^3,\ \mathbf{0}\,\text{m/s},\ 95\,\text{kPa}]^T$. The turbulence is modeled using the LES (Large Eddy Simulation) model, with a damping of the turbulent viscosity towards the walls (Garnier et al., 2009). Two stages are used for the sliding-mesh strategy. In order to increase the accuracy in the satisfaction of the non-penetration condition over the wall when the boundary condition is weakly imposed, the term given by eq. (21) is added to the formulation. $\epsilon = 1 \times 10^{-6}$ is used to compute matrix $\mathbf{M}^*$ (see eq. (22)).
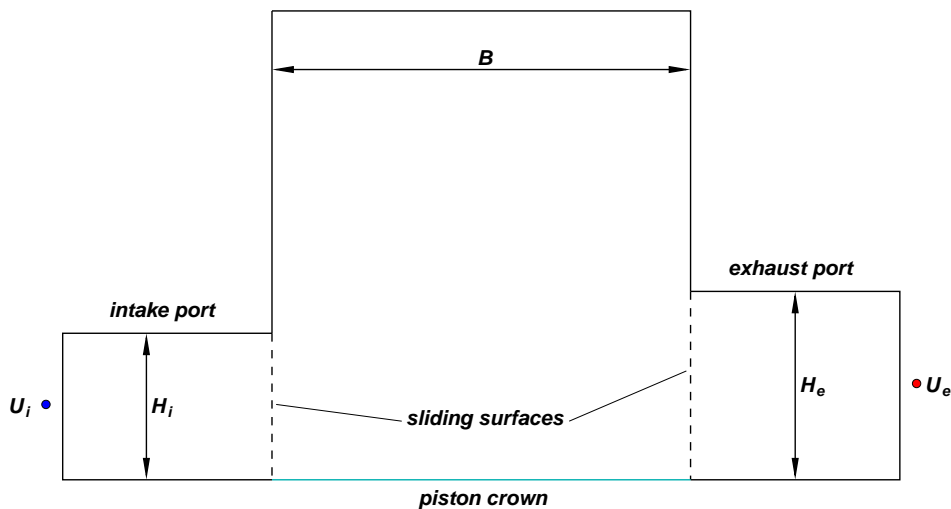
Figure 10: Outline of the geometry of the two-dimensional two-stroke engine.

Results are presented for the open cycle phase only, and correspond to the third simulated cycle. Figure 11 shows the modulus of the flow velocity field and the pressure field for some crank angles during the opening of the ports. The same flow fields are displayed in Fig. 12 for some crank angles when the ports are closing.

In Fig. 13 the instantaneous mass flow rates through the intake and exhaust ports along the cycle are shown. These mass flow rates are expressed per unit length in the normal direction to the plane. For each angle, the integration was made over the port side and over the cylinder side in order to compare both values. The mass flow rates computed at the cylinder side exceed (in absolute value) the respective mass flow rate at the port side, particularly near the opening and closing angles.

6 CONCLUSIONS

In this work we presented a sliding-mesh strategy based on the utilization of continuous finite elements in the interior of the sub-domains and a discontinuous formulation across the interface between these sub-domains. The strategy is applicable to solve compressible viscous flow problems in moving domains, where an Arbitrary Lagrangian Eulerian method is used to account for the movement of the boundary domain. At the discontinuous interface the fluxes are replaced by numerical fluxes, which, in this work, were computed with the Lax-Friedrichs method. The strategy employs a strip of elements, with one of its faces lying on the interface, in order to compute the gradient of the shape function at that interface. Due to the movement of the domain boundaries, some elements that belongs to the discontinuous interface can change its relative position from the interior of the domain to the boundary. For those elements a re-definition of the numerical fluxes that accounts for the boundary condition was proposed. Both, wall and free-stream boundary conditions were considered in this work. The tests presented include two-dimensional compressible flow problems, some of which were solved applying both, the discontinuous strategy proposed here and a continuous formulation in order to compare the solutions. The solution in one of these tests presents strong shocks, which interact with the wall and among them. In general, there is a good agreement between the solution of the continuous formulation and the solution of the discontinuous strategy, particularly when two or more stages are used in the solution algorithm. Also a motored two-stroke engine problem was solved, where the sliding-mesh strategy was applied for the simulation of the opening and
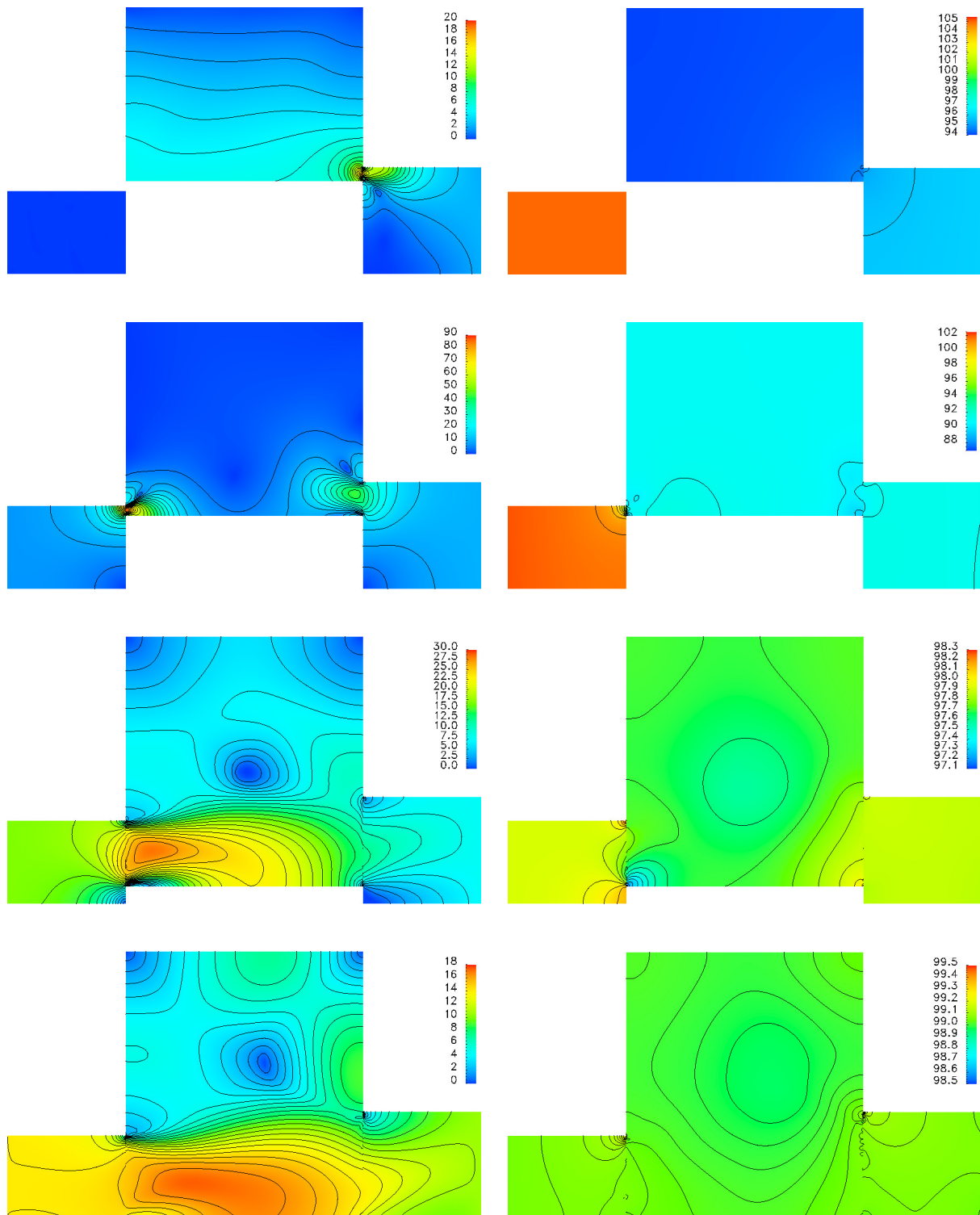
Figure 11: Velocity modulus field (left, in [m/s]) and pressure field (right, in [kPa]) during the port opening phase for the two-stroke engine problem. From top to bottom, crank angles 90°, 100°, 140°, and 180°.

closing of the intake and exhaust ports. Currently, we are working on the application of the strategy to the simulation of three-dimensional geometries of internal combustion engines with ports and turbomachinery.
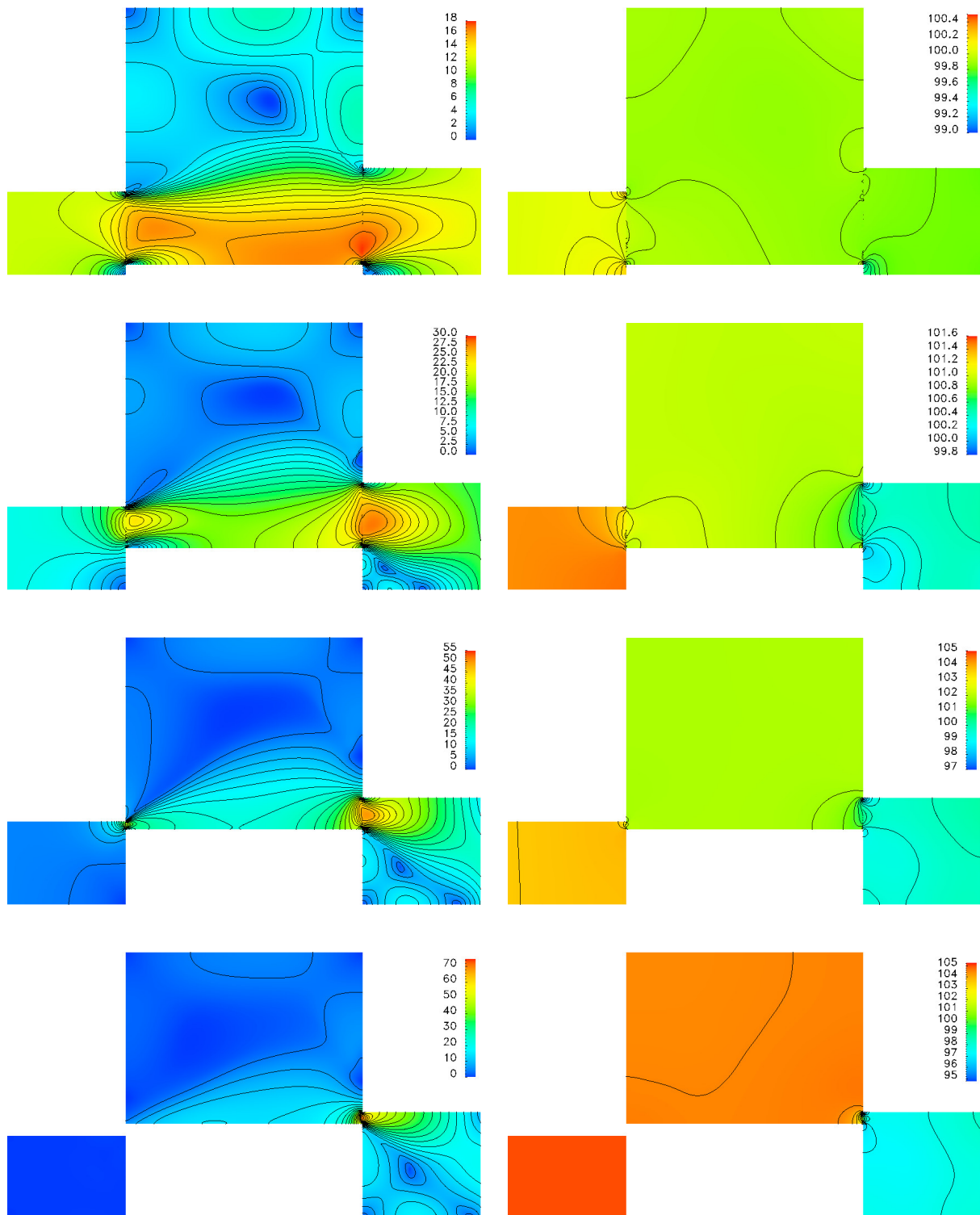
Figure 12: Velocity modulus field (left, in [m/s]) and pressure field (right, in [kPa]) during the port closing phase for the two-stroke engine problem. From top to bottom, crank angles 210°, 240°, 260°, and 270°.

ACKNOWLEDGMENTS
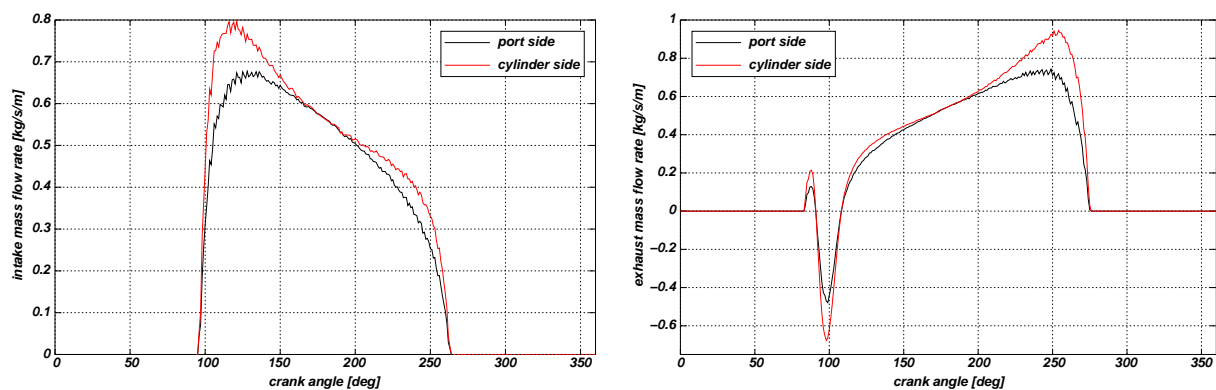
Figure 13: Mass flow rates per unit length through the intake (left) and exhaust (right) ports for the two-stroke engine problem.

REFERENCES

Aliabadi S., Ray S., and Tezduyar T. SUPG finite element computation of viscous compressible flows based on the conservation and entropy variables formulations. *Computational Mechanics*, 11:300–312, 1993.

Amsden A. KIVA-3: A KIVA program with block-structured mesh for complex geometries. Technical Report, Los Alamos, New Nexico, 1993.

Atkins H. Continued development of the discontinuous Galerkin method for computational aeroacustic applications. *AIAA Journal*, pages 97–1581, 1997.

Bernardi C., Maday Y., and Rapetti F. Basics and some applications of the mortar element method. *GAMM-Mitt.*, 28(2):97–123, 2005.

Cai X.C., Dryja M., and Sarkis M. Overlapping nonmatching grid mortar element methods for elliptic problems. *SIAM Journal on Numerical Analysis*, 36:581–606, 1999.

Carnes B. and Copps K. Thermal contact algorithms in SIERRA mechanics; mathematical background, numerical verification, and evaluation of performance. Technical Report, Sandia National Laboratories, 2008.

Choi Y.H. and Merkle C. The application of preconditioning in viscous flows. *Journal of Computational Physics*, 105:207–223, 1993.

Cockburn B., Karniadakis G., and Shu C. *Discontinuous Galerkin Methods: Theory, Computation and Applications*, chapter Discontinuous Galerkin Methods, pages 3–50. number 11 in Lecture Notes in Computational Science and Engineering. Springer-Verlag, New York, 2000.

Collis S. Discontinuous galerkin methods for turbulence simulation. In R.U. Center for Turbulence Research, editor, *Summer Program 2002*. Houston, TX 77005, USA, 2002.

Domino S. Towards verification of sliding mesh algorithms for complex applications using MMS. In R.U. Center for Turbulence Research, editor, *Summer Program 2010*. Houston, TX 77005, USA, 2010.

Donea J., Giuliani S., and Halleux J. An arbitrary, Lagrangian-Eulerian finite element method for transient dynamic fluid-structure interactions. *SIAM Journal on Scientific Computing*, 33:689–700, 1982.

Garnier E., Adams N., and Sagaut P. *Large Eddy Simulation for Compressible Flows*. Springer Science+Business Media, London, 2009.

Hirsch C. *Numerical Computation of Internal and External Flows. Volume 2: Computational Methods for Inviscid and Viscous Flows*. John Wiley & Sons, 1990.

Li B. *Discontinuous finite elements in fluid dynamics and heat transfer*. Springer-Verlag, London, 2006.

López E. *Methodologies for the numerical simulation of fluid flow in internal combustion engines*. Ph.D. thesis, Facultad de Ingeniería y Ciencias Hídricas, Universidad Nacional del Litoral, 2009.

López E., Nigro N., Sarraf S., and Márquez Damián S. Stabilized finite element method based on local preconditioning for unsteady compressible flows in deformable domains with emphasis on the low mach number limit application. *International Journal for Numerical Methods in Fluids*, 69(1):124–145, 2012.

López E., Nigro N., and Storti M. Estrategia de precondicionamiento local para flujos compresibles a bajos números de Mach. *Mecánica Computacional, Volumen XXVII*, 2008.

Mount D. and Arya S. ANN: A Library for Approximate Nearest Neighbor Searching. http://www.cs.umd.edu/~mount/ANN/, 1998-2010.

Rai M. Navier-Stokes simulations of rotor/stator interaction using patched and overlaid grids. *Journal of Propulsion and Power*, 3(5):397–396, 1987.

Sánchez-Caja A., Rautaheimo P., Salminen E., and Siikonen T. Computation of the incompressible viscous flow around a tractor thruster using a sliding-mesh technique. Seventh International Conference on Numerical Ship Hydrodynamics. France, 1999.

Steijl R. and Barakos G. Sliding mesh algorithm for CFD analysis of helicopter rotor-fuselage aerodynamics. *International Journal for Numerical Methods in Fluids*, 58(5):527–549, 2008.

Storti M., Nigro N., Paz R., and Dalcín L. Dynamic boundary conditions in computational fluid dynamics. *Computer Methods in Applied Mechanics and Engineering*, 197:1219–1232, 2008.

Tezduyar T. and Senga M. Determination of the shock-capturing parameters in SUPG formulation of compressible flows. In T.U. Press and Springler-Verlag, editors, *Computational Mechanics WCCM IV*. Beijing, China, 2004.

Wilcox D. *Turbulence Modeling for CFD*. D C W Industries, 2nd edition, 2002.

Woodward P. and Colella P. The numerical simulation of two-dimensional fluid flow with strong shocks. *Journal of Computational Physics*, 54:115–173, 1984.